Periodic Arrays of Diamond-Shaped Silver Nanoparticles: From Scalable Fabrication by Template-Assisted Solid-State Dewetting to Tunable Optical Properties

Paul Jacquet, Barbara Bouteille, Romain Dezert, Joseph Lautru, Renaud Podor, Alexandre Baron, Jérémie Teisseire, Jacques Jupille, Rémi Lazzari, Iryna Gozhyk

WILEY-VCH

DOI: 10.1002/ ((please add manuscript number))
Article type: Full Paper

Periodic arrays of diamond-shaped silver nanoparticles: from scalable fabrication by template-assisted solid-state dewetting to tunable optical properties

*Paul Jacquet, Barbara Bouteille, Romain Dezert, Joseph Lautru, Renaud Podor, Alexandre Baron, Jéremie Teisseire, Jacques Jupille, Rémi Lazzari et Iryna Gozhyk**

((Optional Dedication))

Dr. P. Jacquet, B. Bouteille, Dr. I. Gozhyk
SVI UMR 125 CNRS/Saint-Gobain, Saint-Gobain Research Paris, 39 quai Lucien Lefranc, 93303 Aubervilliers, France
E-mail: Iryna.gozhyk@saint-gobain.com
R. Dezert, Dr. A. Baron
CRPP, Université de Bordeaux, 115 avenue Schweitzer, 33600 Pessac, France
J. Lautru, Dr. R. Podor
Institut de Chimie Séparative de Marcoule, UMR 5257 CEA-CNRS-UM-ENSCM, Site de Marcoule, F-30207 Bagnols-sur-Cèze, France
Dr. J. Teisseire
Saint-Gobain Research Paris, 39 quai Lucien Lefranc, 93303 Aubervilliers, France
Dr. J. Jupille, Dr. R. Lazzari,
CNRS, Sorbonne Université, Institut des NanoSciences de Paris UMR7588, 4 place Jussieu, F-75252 Paris

Keywords: anisotropic nanoparticles, dewetting, localized surface plasmon, lattice mode, silver

Periodic arrays of anisotropic silver nanoparticles having peculiar optical properties are fabricated at a macroscopic scale. The proposed scalable method is based on temperature-assisted solid-state dewetting of a continuous thin layer deposited on a silica substrate patterned by the nanoimprint technique. The resulting nanoparticles are shaped like diamonds and are half–embedded into the patterned silica. A period-dependent optimum in film thickness for the quality of spatial organization is found and discussed in terms of thermodynamics and of the role of grains in the dewetting process. The optical properties of the arrays are driven not simply by the particle shape but also by the lattice period and the degree of order. A surface lattice resonance that disperses with the underlying period is

evidenced experimentally and confirmed by optical simulations. The opportunity to fabricate and tune such an assembly of plasmonic particles on transparent substrate opens interesting perspectives not only for fundamental photonics but also for potential optical applications.

1. Introduction

Surface plasmons are collective oscillations of charge density that occur in materials having a dielectric constant with a negative real part, which is characteristic of metals and some doped semiconductors. Coupling of light to such modes results in marked resonances in the optical properties leading for instance to enhanced absorption or scattering. Plasmonic resonances in nanoparticles, referred to as localized surface plasmons (LSPR), are among the few plasmon excitations which can be probed by direct illumination, unlike guided surface plasmon polaritons that usually require a near-field coupling scheme of some kind. The sensitivity of LSPR at the nanoscale to particle shape and environment gives rise to countless potential applications of nanoplasmonics, such as scattering back-reflector in photovoltaic cells[1, 2], coloration[3], sensors (detection down to 100 femto-mole concentrations [4,5]), photocatalysis[6] and thermal plasmonics[7] as well as perfect absorbers with film-coupled plasmonic nanoparticles[8].

Another way to influence LSPRs in nanoparticles is by bringing them in close vicinity to one another to create coupled modes via resonant plasmon scattering. It is also possible to generate constructive interferences of the scattered fields of all the nanoparticles in an arrangement, also referred to as surface lattice resonances (SLR) or superlattice resonances in case of hierarchical arrays[9, 10]. These collective resonances can impact the existing LSPR of the isolated object or even give rise to new features in the optical response of the particle assembly. It has been shown both theoretically and experimentally, that the optical response of the whole system can be fine-tuned by appropriately designing the geometry of the arrangement of the plasmonic objects such as controlled changes in symmetry or in inter-

particle distance for instance. However, such a control requires mastering the elaboration of samples with large active surfaces.

Nowadays, plasmonic nanoparticles can be produced in many different ways [11, 12] including chemical synthesis from precursors and direct fabrication on surfaces through either growth [13, 14], self-assembly[15, 16] or top-down fabrication methods. Nanoparticle preparation through chemical synthesis is extremely versatile in terms of both materials (metals, plasmonic oxides etc.) and shapes [17, 18] (spheres, pyramids, javelins etc.) with an accurate control of size. Yet, in order to use such synthetized nanoparticles, an additional transfer step of the nanoparticles from the jar to the final arrangement on a substrate or within a volume without agglomeration is required, which is not at all straightforward. This step is paramount in the fabrication process to achieve the tailored optical properties of the structure [19]. The direct deposition of nanoparticles on surfaces by oblique angle deposition [13] or pulsed laser deposition[14] fails to fully control the arrangement of the grown nanoobjects. The three different types of techniques that are generally applied for designing arrangements of nanoparticles on surfaces are: (i) self-assembly techniques, such as nanosphere lithography[15], (ii) top-down methods that involve e-beam[20]/photolithography followed by lift-off or laser assisted tools like laser-induced backward[21] or forward[22] transfer, and finally (iii) self-assembly assisted by preliminary top-down step, such as directed self-assembly[16]. The main advantage of self–assembly techniques is their scalability, although this comes quite often at the cost of prohibitively dense defects in the final structure. Top-down methods allow for a very precise control of the position and the size of each nanoparticle, but only arrays of a few millimetres in size are achievable within relatively reasonable fabrication time and cost. In their basic configuration, both self-assembly and top-down methods give rise to quasi-2D structures (discs, prismatic nanoparticles, etc.). Recent progress in metamaterials show that more sophisticated anisotropic shapes can in principle be obtained but this requires complex

fabrication routines extremely sensitive to the quality of lateral alignment between elaboration steps. For example, L-shaped nanoparticles reported by Odom *et al.* [9] required two-step lithography, while fabrication of 3D nanoparticles with concavities such as U-shaped[23] particles is even more challenging since it requires lithography steps at each layer in the stack.

An interesting alternative to these methods of elaboration is given by solid-state dewetting[24]. This phenomenon is a temperature-triggered solid transformation of a continuous thin film towards disconnected agglomerates. It is thermodynamically driven from the metastable continuous film state and happens at temperatures below the material melting point. Due to confinement at the surface of the substrate, both diffusion on the free surface of the film and at the interface with the substrate[25] can participate in the process. Mechanisms and kinetics of dewetting depend on the nature of both the film and the substrate (crystalline or amorphous) as well as on the annealing atmosphere[26]; they have been studied in particular for films of the platinum group[27, 28] and of noble metals[26, 29, 30, 31, 32, 33, 34, 35]. Yet, in the case of complex polycrystalline film on amorphous flat substrates, recent studies using various *in situ* and real time measurement imaging techniques have shed light on the major role played by grains in the kinetics of dewetting and in the evolution of the coverage/density of objects and holes[26, 31]. The particles obtained in such cases have a large size dispersion[2, 36], while their shapes may vary from faceted truncated spheres [31] to complex worm-like objects [26, 36]. Several schemes can be leveraged to influence the dewetting process and therefore the final morphology, namely: (i) modification of either the nature of the substrate or of the annealing atmosphere [26] that impact the diffusion constants and (ii) annealing conditions (furnace, laser heating, [3], microwave annealing etc.). But, in this context to really guide dewetting towards an organized configuration, the best method is surface patterning, as demonstrated by Giermann and Thompson[29,30] for gold films on silicon substrates. This method relies on the local curvature gradient created in the metallic layer by the surface pattern. Such a gradient

enables to locally guide the dewetting in order to fill or avoid valleys in the pattern[29,30]. This method proved extremely versatile in terms of metals (Co[37] or Au[29,30] on patterned silicon), shapes or patterning methods (such as honey-comb quasi-periodic lattices obtained with nano-sphere lithography [38]). Curvature gradient can also be achieved by post-patterning the metallic layer [39]. Such a method applied to single-crystal films on crystalline substrates paves the way to a wide range of nanoparticle shapes, as it was shown for the dewetting of post-patterned epitaxial Ni[40, 41] and Pd[41] films grown on single-crystal MgO substrates by adjusting the crystallographic orientation of metal films during growth.

To overcome the inability of the currently used methods to produce scalable large arrays of plasmonic particles with tailored optical properties on glass-based transparent substrates, the present work proposes to combine nano-imprint lithography of silica sol-gel with solid-state dewetting of silver, a well-known plasmonic material at optical frequencies. With silver, relatively low temperatures (around 400 °C) are required to reach the final arrangement of objects. Yet, the driving forces underlying organization of silver, the levers of control and the impact on the optical properties remain largely unexplored. Preparing films of tailored properties requires establishing a clear relationship between the original object (namely the surface pattern, the film thickness and its polycrystalline structure), the final morphology (namely, the shape of the object and the spatial organization) and the properties of interest. The present paper is organized as follows: after a description of the method that allows fabricating arrays of diamond-shaped silver nanoparticles, a dedicated algorithm of treatment of scanning electron microscopy images is introduced to judge the quality of dewetting. It is shown that, under identical conditions of deposition and dewetting, an optimal initial film thickness for organization does exist; arguments based on thermodynamics and on grain density are put forward to explain this finding. Periodic arrangements of nanoparticles can be routinely achieved at the cm-scale, though with 25-30% of particles which do not perfectly

follow the pattern. Electromagnetic simulations help assigning the observed optical features not only to the half silica-embedded diamond-shape but also to the long-range periodic arrangement. A “surface lattice resonance” is clearly identified and its tunability by adjusting the period of the pattern is demonstrated.

2. Scalable fabrication of arrays of diamond-shaped silver nanoparticles via solid-state dewetting

Solid state dewetting of thin films deposited on flat surfaces results in the formation of a random ensemble of nanoparticles of, at best, similar shape but large dispersion in sizes[24, 26, 42, 43]. In their pioneering work, Giermann and Thompson[29] suggested guiding the dewetting through surface patterning to achieve organized arrays of objects, more precisely by creating an arrangement of pits on a flat surface by lithography prior to the deposition of the thin film to be dewetted. The pits, shaped as inversed pyramids, are both relatively simple to produce through chemical etching of a crystalline silicon substrate and compatible with conformal deposition.

The present fabrication method is derived from this initial idea but is based on the nano-imprint technique with the advantage of being applicable to any material (provided its availability as a sol-gel), as well as scalable and feasible on any substrate, in particular transparent ones that allow a wide variety of optical characterizations. It consists in three steps (Figure 1, experimental section) involving patterning of a glass substrate, deposition of a conformal thin silver layer and dewetting through annealing. Basically, the nano-imprint lithography technique is applied to replicate an existing patterned silicon surface (the master) on silica sol-gel films deposited on a glass substrate (Figure 1, left). The surface of the reusable master mould is covered with inverted pyramids engraved by lithography and

chemical etching (see Figure 1, details are given in the experimental section) and arranged into a square periodic lattice of period P = 200, 350, 500, 600 or 750 nm (Table 1). The negative of the master surface is replicated by moulding a polydimethylsiloxane (PDMS) polymer layer, which is then used for nano-imprinting a freshly spin-coated silica sol-gel layer[44]. To understand the effect of the surface patterning on metal dewetting, reference flat surfaces of sol-gel silica were also prepared by replacing in the process the master by a standard flat silicon wafer. As a result, the impact of the support material on the dewetting process is excluded since silver is deposited on surfaces of different morphologies but of identical nature. Polycrystalline conformal silver films of thicknesses ranging between 10 and 80 nm were deposited by magnetron sputtering on top of the patterned sol-gel surfaces (Figure 1, centre). Finally, solid state dewetting of silver was induced by annealing at 400 °C in ambient air during 2 hours in an oven (Figure 1, right).

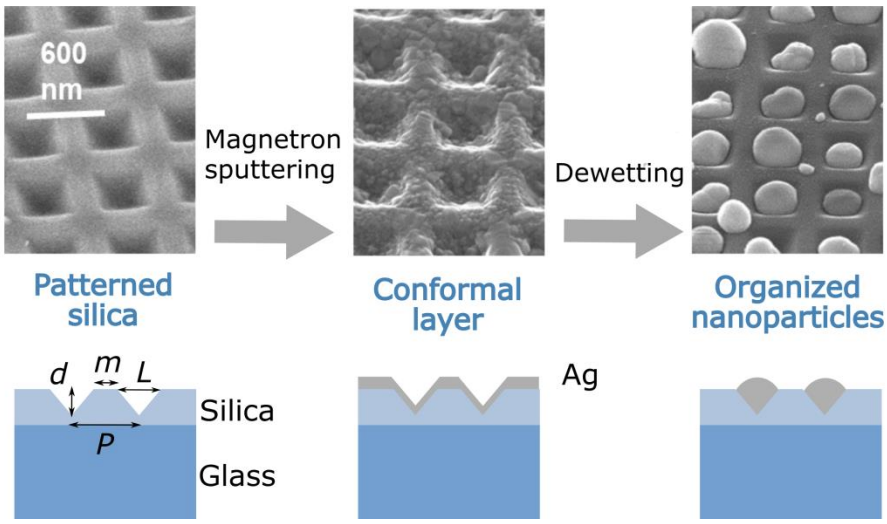

Figure 1. Scheme of the fabrication protocol. Bottom panel: side view sketch defining mesa size *m*, pit depth *d*, pit size *L* and lattice period *P*; top panel: corresponding SEM images with a slight tilt.

The morphology of the samples and of the masters was examined at different stages of the fabrication process by scanning electron microscopy (SEM). Plane views were used to observe particle sizes and ordering while the particle profile was apprehended by grazing-

incidence SEM on sample cross-sections. On the flat surface (Figure 2-a), the particle profile is close to a truncated sphere, the expected equilibrium shape of a metal as silver with a poor surface energy anisotropy[45]. The contact angle, close to $\Theta_e = 90°$, is larger than expected ($\approx 130°$) from surface and interface energies in vacuum of silver and silica[46] but in agreement with previous studies on the influence of oxygen adsorption on silver/oxide wetting[43,47]. Figure 1 may give the feeling that silver nanoparticles dewetted into the pits of the silica pattern have a spheroidal profile. But SEM images of the vertical cross-section of the sample shown in Figure 2-b reveal a more complex diamond-like shape. In contrast to previous reports on gold dewetted directly into silicon pits[29,30], the upper spherical parts of the present particles protrude well above the surface while the lower part, embedded in silica, has a more conical shape. As previously shown[42,44] and confirmed herein by atomic force microscopy (AFM), PDMS moulding, nano-imprinting and annealing smoothen partly the initial pyramidal shape of the silicon master as shown by the pit depth change between master and silica layer (Table 1). As seen below, this diamond-like shape yields a specific optical response.

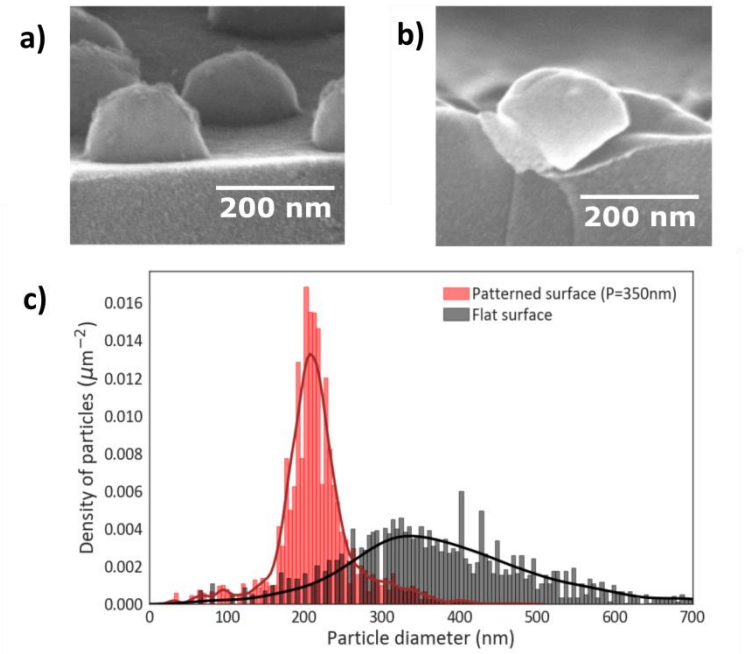

Figure 2. Shape of dewetted nanoparticles: typical SEM snapshot of a cross-section of a thin silver layer dewetted on a) flat and b) patterned surface; c) dispersion of the in-plane dimensions the nano-particles obtained after dewetting of a 30 nm Ag film deposited on flat and patterned surface (P=350nm, square lattice).

Table 1. Geometrical parameters of patterned surfaces defined in Figure 1 as measured by AFM.

Period [nm]	Mesa [nm]	Depth [a)] [nm]	Depth [b)] [nm]
200	75	90	25
350	135	150	80
500	130	260	170
600	150	315	170
750	190	394	295

[a)] of pyramids in master; [b)] of pyramids in sol-gel layer after annealing.

To quantify the degree of lateral ordering of the particles on patterned surfaces, a dedicated image processing was developed (Figures 3-4). The main steps were the image segmentation, the detection of the mass centre of the particles and the analysis of size and position of each particle with respect to the closest lattice node. All particles at a distance more than 0.25 P

from the closest lattice node were considered as misplaced (coloured in blue in Figure 3-a). Particles with projected areas greater than that of the basis of the inverted pyramid (coloured in red in Figure 3-a) were assumed to be too large. Objects on the edges of the SEM images were excluded from the statistics (coloured in grey in Figure 4). The analysis was performed on SEM images with a large field of view (Figure 4) leading to, at best, statistical data on close to 750 particles (Figure 4-c). The quality of the ordering was characterized through the ratio of the number N of particles of appropriate size and position found on an image (coloured in green in Figures 3 - 4) to either the total number of particles $n_t = \frac{N}{N_{part}}$ or the total number of unit cells $n_h = \frac{N}{N_{holes}}$. Plotted as a function of the initial layer thickness in Figure 3-b, these two parameters describe the accuracy at which dewetting follows the initial pattern. For instance, if the total number of particles exceeds the total number of unit cells on the image, $n_t < n_h$; the crossing of these two curves indicates the optimal initial thickness of the film at which dewetting gives rise to one particle per unit cell. This value corresponds to the best quality achievable and depends on the period and lattice type (see Table 2). However, if at best 20% of the particles are still of inappropriate size or misplaced (Figure 3-c) on the patterned surface, the dewetting of the silver films on the flat silica surfaces results in an ensemble of randomly distributed particles with a large dispersion in size (Figure 2-c) in agreement with former results on polycrystalline films on amorphous substrates[2, 36]. This observation leaves open the question of the main driving force behind organization on patterned surfaces.

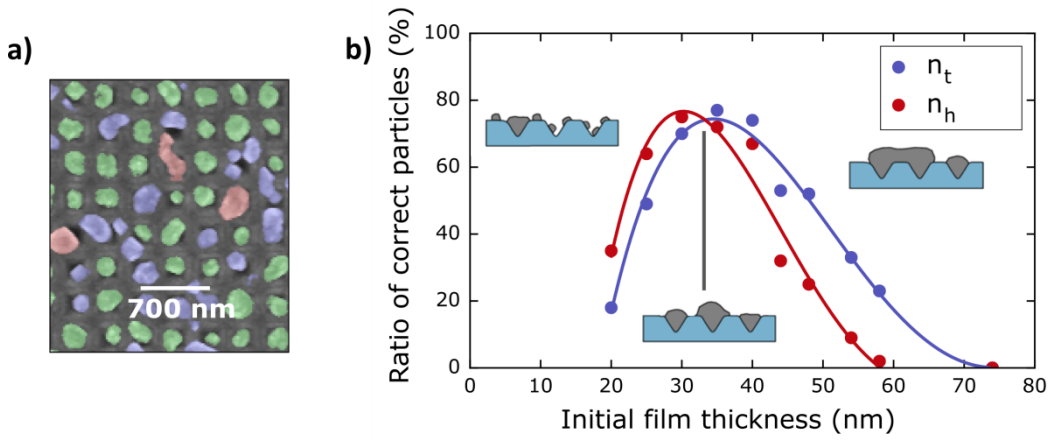

Figure 3. Illustration of the image processing algorithm: a) Example of a treated SEM image of dewetting; nanoparticles coloured in green are of correct size and position, in red of incorrect size, and in blue of correct size but misplaced (see text for definition); the period is P=350 nm. b) Quality of the obtained array of particles as determined by the algorithm: ratio of particles of appropriate size and position normalized by the total number particles n_t (blue disks) or by the number of unit cells n_h (red disks) as a function of the initial thickness of the layer (see Figure 4). Lines are to guide the eyes. The arrow points at the optimal thickness in term of organization.

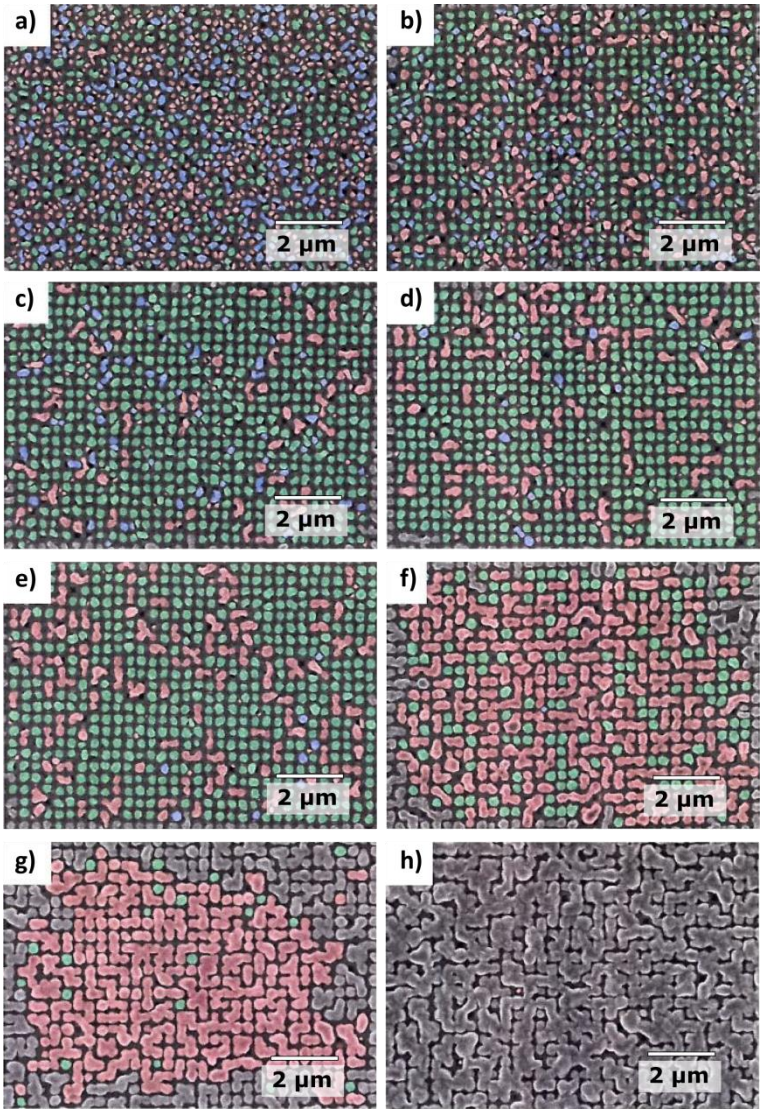

Figure 4. SEM images (11.5 x 8 µm^2) of structures obtained after dewetting of a silver layer deposited on a patterned silica surface (square array, period 350 nm). Layers of different initial thickness are compared: a) 20 nm; b) 25 nm; c) 30 nm ; d) 35 nm ; e) 40 nm; f) 45 nm; g) 55 nm; h) 75 nm. Particles are coloured accordingly to the image analysis algorithm described in the text (see Figure 2). Particles in grey are excluded in the treatment since they touch the border of the image. The limit of the volume conservation rule is $t_{lim} \cong 10$ nm (see text for definition).

Table 2. Optimum thickness of Ag thin film for patterns with different periods.*Calculated based on volume conservation rule from[42,43] , suggesting that film volume corresponds to the pit volume $t_{lim} = \frac{d}{3}\left(1 - \frac{m}{P}\right)^2$.** Calculated based on volume conservation rule, suggesting

that film volume corresponds to the volume of a diamond with its cone part filling the pit and upper part being a half-sphere $t_{lim} = \frac{2\pi}{3} L \left(\frac{L}{P}\right)^2 \left(1 + \frac{d}{2L}\right)$.

Period [nm]	Experimental optimum thickness [nm]	Calculated optimum thickness, allowing to fill the pyramid [nm]*	Calculated optimum thickness, allowing to form a diamond** [nm]
200	-	3.3	15.3
350	33	10.1	29.1
500	44	31	77.4
600	52	31.9	91.3
750	68	54.8	124.8

3. Parameters impacting template-assisted solid-state dewetting

Although the minimization of surface/interface energies is at work during dewetting of a thin film of a given solid material, controlling the final morphology requires both favouring a given structure on a thermodynamic point of view and worrying about the dynamics of the phenomenon. In fact, based on the important role played by grains in the dewetting process on flat surfaces [26, 31], the control of dewetting through the substrate patterning should not solely rely on the geometry of the pattern but also on the average dimensions of the grains in the initial polycrystalline film.

In their pioneer work[29,30] on template-guided dewetting of metal films, Giermann and Thompson suggested that the organization is ruled by simple geometrical considerations based on volume conservation. In order to fill all the pits, the volume tS deposited per unit cell must be smaller than the volume of a single inverse-pyramid $V_{hole} = \frac{4}{3} dL^2$. The parameter $t, S, d, L = \frac{1}{2}(P - m), m$ and P stand respectively for the initial film thickness, the area of the unit cell ($S = P^2$ for a square lattice), the depth of the pits, their lateral size, the mesa extension and the period of the pattern (see Figure 1-a). Giermann and Thompson defined a limit film thickness $\frac{t_{lim}}{d} = \frac{1}{3}\left(1 - \frac{m}{P}\right)^2$ above which all the particles are in the pits while above

that limit the film escapes the underlying pattern. A combination of these two morphologies is expected and observed in the case of gold on patterned silicon for thicknesses close to t_{lim}[29,30]. However, the present system of silver/silica clearly does not follow this volume conservation rule. As shown in Figure 4 for patterned surfaces with a 350 nm period, the initial film thickness does impact the final morphology of the dewetted films. Curiously, the smallest thickness in this set of experiments (Figure 4-a) was about $2t_{lim}$ and resulted in dewetting with several particles per hole. The best dewetting quality is observed for thicknesses ranging between $3.5t_{lim}$and $4t_{lim}$ (see Figure 2-b and Figure 4-c,d) that is to say for a volume of metal much larger than that of the inverse pyramid. Finally, the dewetting of films thicker than the optimum $3.5t_{lim}$ leads to a dominant population of nanoparticles connecting several pits.

3.1. Energetic aspects and preferential growth in the pits

To address the relative thermodynamic stability of a diamond-shaped particle (state A, Figure 5-a) and of a particle on a flat mesa (state B, Figure 5-a), the former is assumed to have a conical-embedded shape (as done later on for the optical simulations) and the latter to be in the form of a truncated sphere with an equilibrium contact angle Θ_e (Figure 2-a). Beyond allowing tractable calculations, the conical rounding of the square pit is a fair hypothesis in light of the smoothing of the initial pyramidal shape during the elaboration process. For a given volume of metal, the variation of energy between configurations A and B can be expressed through the surface/interface energies γ and the involved surface areas S :

$$\Delta E_{AB} = \gamma_m S_{sph,B} + \gamma_{ms} S_{int,B} + \gamma_s S_{co} - \gamma_m S_{sph,A} - \gamma_{ms} S_{co} - \gamma_s S_{int,B} \quad (1)$$

where indexes *m* stands for metal, *s* for the silica, *ms* for their interface, *sph* for the spherical part of the object, *int* for its interface with the substrate and *co* for the conical part of the particle (Figure 5-a). Each term describes the creation or disappearance of the

surface/interface when going from A to B configurations. The Young-Dupré equation $\gamma_{ms} = \gamma_s - \gamma_m \cos\theta_e$ allows to further simplify the equation:

$$\Delta E_{AB}/\gamma_m = S_{sph,B} - S_{sph,A} - \cos\theta_e\, S_{int,B} + \cos\theta_e\ S_{co} \quad (2)$$

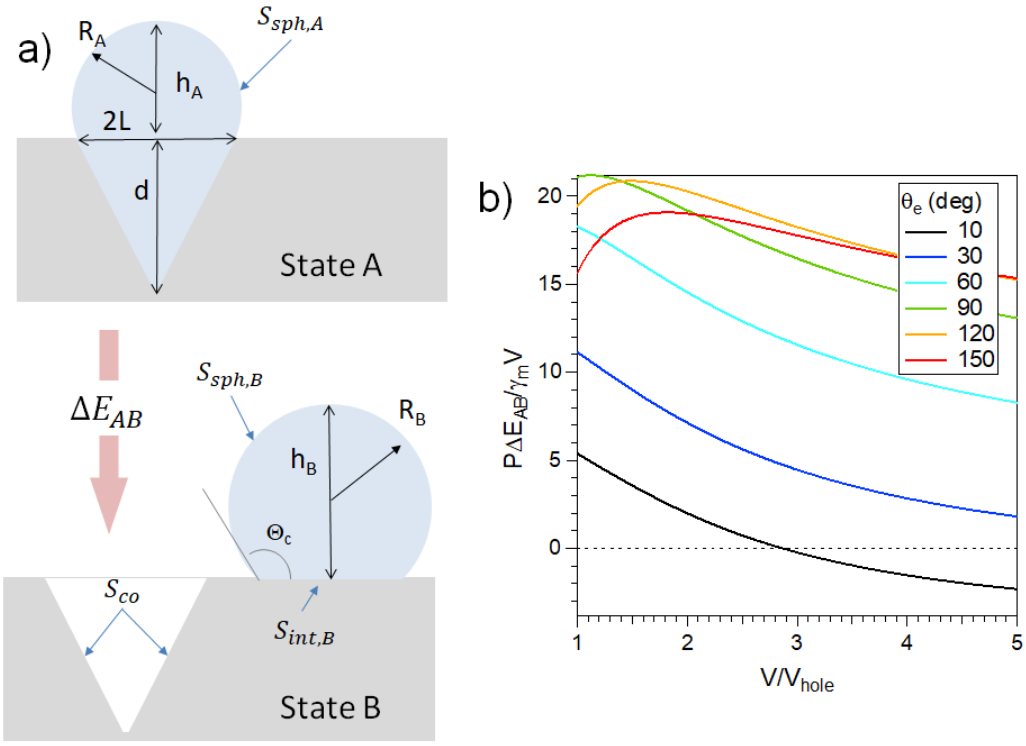

Figure 5. Relative thermodynamic stability of particle in a pit and on a mesa: a) Morphology configurations; the pit is approximated by a cone and the particle on a flat mesa is a truncated sphere at equilibrium contact angle θ_e. b) Normalized variation of energy between A and B configurations as a function of the total volume for various values of angle θ_e. See text for the definitions of the parameters.

Under the condition of volume conservation $V = V_{sph,B} = V_{sph,A} + V_{co}$ and using the expressions of the volumes and the surfaces of a truncated sphere of height *h* and of a cone of radius *L* and depth *d*:

$$S_{sph} = 2\pi Rh, \quad (3)$$

$S_{int} = \pi h(2R - h)$, (4)

$V_{sph} = \pi\left(Rh^2 - \frac{1}{3}h^3\right)$, (5)

$S_{co} = \pi\sqrt{d^2 + L^2}\,L$, (6)

$V_{co} = \frac{1}{3}\pi d\,L^2$, (7)

the adimensional energy variation $P\Delta E_{AB}/\gamma_m \mathrm{V}$ was calculated as a function of the volume of matter V normalized to the volume of the hole $V_{hole} = V_{co}$ for different conditions of wettability given by Θ_e. As shown in Figure 5-b for the case of the P=350nm pattern (Table 1), the particle in the pit is systematically more stable than the particle on the mesa, except in the case of extremely good wetting. But, according to Figure 2-a, the silver/silica case (annealed in oxygen) corresponds to $\Theta_e = 90°$; the excess of matter above $V_{hole} = V_{co}$ (or of thickness above t_{lim}) is more stable in the pit up to very large values. This lies in the energetically favourable formation of a metal/silica interface in the cone. The extension (not shown) of this thermodynamic modelling to an arbitrary sharing of volume between the two types of particles with a dewetted partially filled hole shows that this trend is not reversed even for intermediate cases.

3.2. The role of grains

The dynamics of dewetting of thin polycrystalline films involves three successive processes[31]: an induction stage, the propagation of holes and the sintering of isolated particles. During induction, the continuous polycrystalline film undergoes local recrystallizations and grain boundary groovings. During this step, some grains are growing at the expense of others until the first holes appear. Although the selection rule of the grains to grow is still unclear in particular on amorphous substrates as herein, most of the grains obtained at the very end of the dewetting are those selected during the first induction period[31]. Figure 6 shows a sequence of SEM images at different stages of dewetting of a thin silver film

of optimum thickness on patterned silica. A large amount of grains that have grown during the induction stage are already located inside the pits and not on the mesas. Moreover, preferential growth inside the holes is observed even for relatively thick layers (up to 3-5 times t_{lim}).

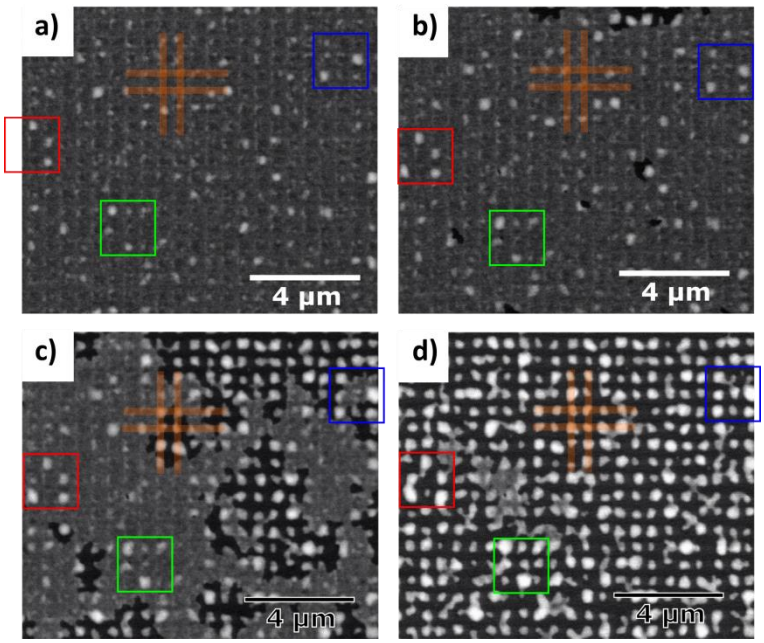

Figure 6. Selection of grains during dewetting on patterned surfaces (P=600 nm, square lattice): SEM images a) during induction stages and b-d) during hole propagation step. As underlined by coloured square boxes, notice in image-a that pits are already decorated by larger grains during induction. The orange cross points at the underlying mesh.

Basic geometrical arguments can help finding out if the density and the size of individual grains in as-deposited films can be at the origin of this effect. If a_{mesa}, a_{pit} are the average lateral dimensions of the grains on the mesas and in the pits, the number of grains per unit cell on the mesa N_{mesa} and in the pyramidal pit N_{pit} can be estimated by straightforward algebra from their respective surfaces:

$$N_{mesa} = \left[\frac{P^2-4L^2}{a_{mesa}^2}\right] \quad (8)$$

$$N_{pit} = \left[\frac{4L\sqrt{L^2+d^2}}{a_{pit}^2}\right] \quad (9)$$

Here [x] stands for the floor function of x which returns the greatest integer less than or equal to its argument x. Assuming an initial conformal film due to normal deposition, the thickness t_{pit} of the film on the slopes of the pyramid is reduced to:

$$t_{pit} = \frac{t}{\sqrt{1+\left(\frac{d}{L}\right)^2}} \quad (10)$$

compared to that deposited on the mesa t. With magnetron sputtering deposition, as a rule of thumb due to columnar growth[48], one grain in the thickness of metallic film is often observed for thicknesses smaller than 80 nm. Even though it can be influenced by deposition parameters to some extent, the average lateral grain size is also of the order of the film thickness. Therefore assuming $a_{mesa} \approx t$ and $a_{pit} \approx t_{pit}$, N_{mesa} and N_{pit} could be evaluated from equations 8-9 for the different used patterns as given in Table 1; as shown in Figure 7-a, the mesa is systematically less populated in terms of grains than pits except for the 200 nm period. Therefore, abnormal grain growth is more likely to happen in the pit than on the mesa. Furthermore, experiments of dewetting of silver on flat silica have shown that the average diameter *D* of the final particles obtained after dewetting is proportional to the initial thickness of the silver layer (Figure 7-b). Assuming a hemisphere shape (Figure 4-a), the average number of grains of size *a* required to build such a particle is given by:

$$N_{hemisphere} = \left[\frac{\pi}{12}\left(\frac{D}{t}\right)^3\left(\frac{t}{a}\right)^3\right] \quad (11)$$

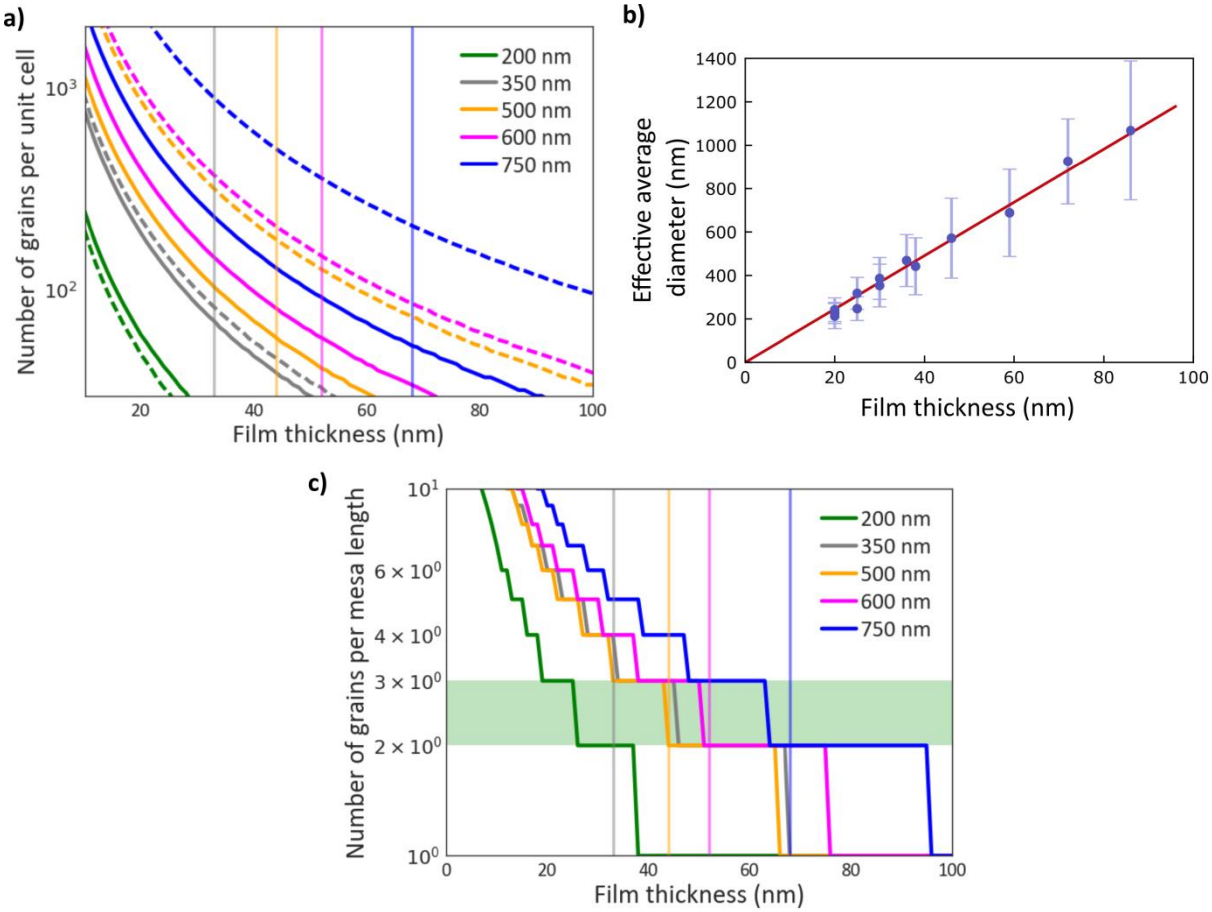

Figure 7. Role of the number of grains in dewetting. (a) Estimated number of grains per unit cell in as-deposited film on mesa N_{mesa} (straight line, equation 8) and inside the pyramid N_{pit} (dash line, equation 9) for square lattice patterns of different periods. (b) Measured average diameter of particles as a function of the initial film thickness after dewetting of silver films on a flat silica surface. (c) Estimated number of grains per mesa length in as-deposited films (straight line, equation 13). Thicknesses corresponding to the best quality of ordering for a given period are shown with vertical lines of the same colour. No such optimum thickness was experimentally found for 200 nm period.

Volume conservation implies that the growth of such a hemispherical particle will consume all the grains from a "capture" area $N_{hemisphere}a^2$. Within the previous hypothesis $a \approx t$, the diameter D_{pump} of the capture area is given by :

$$\frac{D_{pump}}{a} = \left[\frac{D}{t}\sqrt{\frac{D}{3t}}\right] \quad (12)$$

Using the experimental slope of Figure 7-b ($D \approx 12t \approx 12a$), $D_{pump} \approx 24a$. This means that in case of deweting on a flat surface, the final particle can deplete around itself a ring of size $(D_{pump} - D)/2 \approx 6a$. Therefore, a criterion to achieve the best ordering on a patterned surface is that this depletion zone for the particles that could grow on the flat mesa is smaller than the previously found value of 6. Otherwise the excess of grains on mesa will result into the growth of particles on it despite thermodynamics. The evolution of the number of grains per mesa length

$$N_{mesa-1D} = \left[\frac{m}{a}\right] \quad (13)$$

is shown in Figure 7-c within the hypothesis $t \approx a_{mesa}$. Amazingly, the experimentally observed optimum initial thicknesses for each examined pattern corresponds to $N_{mesa-1D} \approx 2-3$ grains, a value below the above mentioned limit of 6 grains in case of dewetting on flat surface. Indeed, in our case local curvature gradient due to the pattern decreases this depletion area.

These rough estimates allow pinpointing the fact that, due to the granular nature of the initial film, there is an optimal thickness range for each period in which close to one particle per pit and per unit cell is more likely to happen.

4. Shape- and lattice-related specific optical properties

Contrary to silicon, the transparency of such glass-based samples allows to illustrate the optical properties through absorption spectra A, estimated from the measured integrated reflectance (R) and transmittance (T) spectra (see experimental section) as $A = 1 - R - T$. Patterning yields to specific and tuneable plasmonic optical properties (Figure 8). The combination of experiments and finite-element numerical simulations unravelled that they are

related not only to the half-embedded diamond-like shape of the silver particles, but also to the formation of long-range ordered array of objects.

While the optical spectra of substrates prior to metal deposition showed very little impact of patterning (Figure 8-a), measurements on the dewetted silver thin film deposited on the flat surface exhibit two nanoparticle-related features (Figure 8-a). The first one appears at a wavelength of about 420 nm and is independent of the dewetting quality and the thickness of the initial film. The second one is located within the near infrared region around 620 nm. It is rather broad, while its position varies with the average size and density of the nanoparticles.

In the case of films dewetted on patterned surfaces, a period-independent peak at about 420 nm is also present, but a second and significantly sharper feature emerges at around 540 nm for P=350 nm (Figure 8-a,b). Amazingly, its spectral position varies linearly with the period of the pattern (Figure 8-b, inset), which is an obvious signature of surface lattice resonances [49] as they occur at wavelengths larger than the maximum resonance wavelength of the single particle constituting the lattice [50]. In fact, the surface lattice resonances in periodic arrangement of nanoparticles are related to absorption of diffractive orders generated at grazing angles, which occur at the so-called Rayleigh cut-off wavelength. Under illumination at normal incidence, Rayleigh cut-off wavelength is proportional to the array period and for a square array reads as:

$$\lambda^{i}_{m_1,m_2} = \frac{n_i}{\sqrt{m_1^2+m_2^2}} P \quad (14)$$

Here index *i* indicates the medium, i.e. substrate (silica) or superstrate (air), where the grazing angle diffraction happens. n_i is the corresponding refractive index; m_1 and m_2 are two integers defining the grating orders along the reciprocal vectors of the square unit cell. In fact, the wavelength of the SLR-related peak in Figure 8-b follows exactly $\lambda^{i}_{0,1}$ (=$\lambda^{i}_{1,0}$) in the substrate (silica, n=1.46).

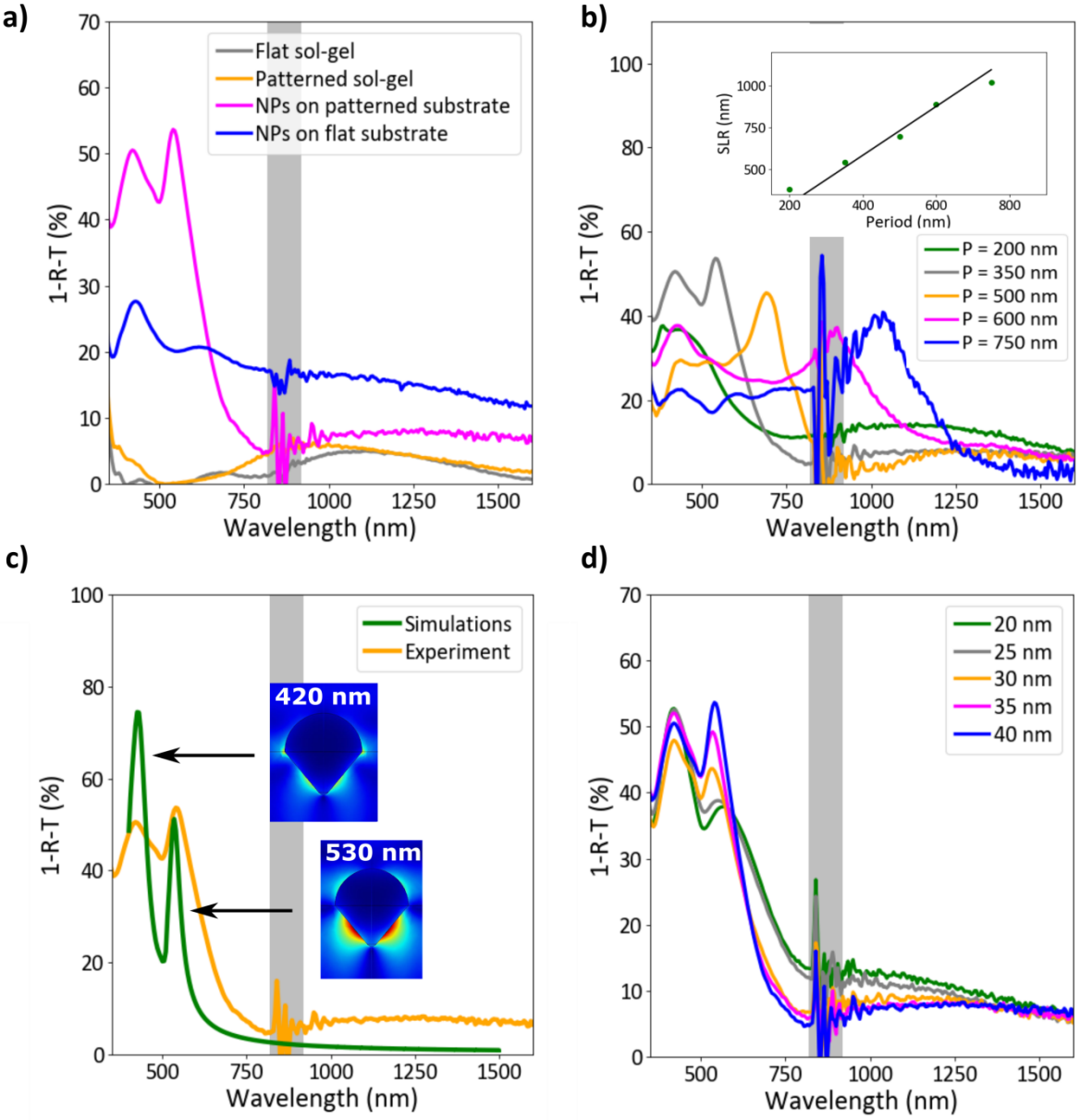

Figure 8. Deduced absorption spectra $A = 1 - R - T$ for flat and patterned nanocomposite films obtained through dewetting of thin films of silver on flat and patterned silica. All experimental spectra were plotted without any smoothing and thereby contain strong noise around 850 nm due to the change of grating in spectrometer (grey box). (a) Comparison of random arrangement of plasmonic nanoparticles and square array with P=350 nm, obtained through dewetting of 35 nm thick Ag film on flat and patterned silica respectively. Measured absorption of the flat and patterned substrates is also shown. (b) Comparison of square arrays of plasmonic nanoparticles obtained through dewetting on patterned silica of different periods.

Position in wavelength of the surface lattice resonance as a function of period is given in the inset. (c) Comparison of absorption deduced from experimental data and obtained with numerical FEM simulations for a square lattice of diamond-shaped silver nanoparticles half embedded into silica (as shown in Figure 1 and Figure 5-a, see Table 1 for dimensions). The insets show the distributions of electric field at the two resonant wavelengths 420 nm and 530 nm. (d) Impact of dewetting quality on the optical properties illustrated for silver films of different thicknesses (between 20 and 40 nm) deposited on a square array pattern of period P=350 nm.

To understand the experimental findings, finite element numerical simulations (see details in experimental section) were performed on perfect periodic arrays of nanoparticles. The objects were given a diamond-like shape matching the experimental finding, but with an embedded conical part. A good agreement with experiments is achieved on the prediction of the positions of absorption peaks (Figure 8-c). Yet SLR-related peak in experimental spectrum is significantly less intense and wider presumably due to the defects in the structure. Field distributions plotted in the inset of Figure 8-c show complex non-dipolar structures of the plasmon modes both at 420 nm and SLR-related peak. Interestingly, the field of the SLR-related peak is mainly concentrated inside the substrate, as expected from equation 14 and the linear dependence of the inset of Figure 8-b.

Optical properties are obviously correlated to the morphology of the dewetted film which is thickness–dependent. Spectra (Figure 8-d) obtained by varying the thickness around the optimum of Figure 2-b turned out to be quite sensitive to the organization, particularly the SLR-related peak. When the film is too thin and dewetting results in several particles per pit or when objects coalesce at large thickness, the second peak in the $A = 1 - R - T$ spectrum considerably broadens. At the opposite, the low-wavelength feature related to the particle

shape is less sensitive to the degree of order. As a result, beyond the tunability of the optical response with the period and thickness, optics can be used to monitor the quality of dewetting.

5. Conclusion

High quality periodic arrangements of diamond-shaped silver nanoparticles could be achieved at macroscopic scale through solid state dewetting of a film deposited on transparent patterned substrates produced by the nano-imprint technique. The conditions of spatial organization of the plasmonics nanoparticles and the impact on the optical properties of the assembly were explored.

A SEM image processing algorithm was developed to quantify the quality of the arrangement of nanoparticles upon dewetting. It allowed identifying an optimum film thickness for a given pattern. Contrary to previous findings for gold on silicon[29,30], the best conditions could be achieved for a metal volume per unit cell well above that of the hole of the pattern in agreement with thermodynamic expectations. As in the case of silver dewetting on flat surfaces, the role of grains in the final organization was pinpointed; the condition for obtaining the best network is to have a grain (and only one) growing inside each pit of the pattern.

While silver particles randomly distributed on the surface of a silica substrate give rise to an absorption peak centred at 420 nm, a new feature at larger wavelength emerges in organized arrays. At the opposite to the 420 mn peak whose energy is assigned to the particle shape, its position varies linearly with the period of the pattern and its sharpness and intensity is correlated to the quality of the arrangement. Numerical simulations allowed to rationalize the experimental findings and the origin of both peaks. The lattice-related feature is assigned to the absorption of a diffraction peak created by the grating and propagating parallel to the surface. On an optical point of view, the proposed synthesis technique overcomes the spatial

limitation of lithography by providing centimetre-sized samples which are suitable for full optical characterization and not only specular reflection as in the case of opaque substrates. The tuning of optical properties of such arrangement of nanoparticles through both the master mold and the nature of the sol-gel material opens a number of interesting perspectives for fundamental optics but also for potential applications.

6. Experimental and theoretical details

Master surfaces for nano-imprint lithography: Patterned silicon surfaces were purchased from CEMITEC company, Spain. The periodic arrangements of square holes were created by electron-beam lithography in a resist layer on top of (100) silicon wafers. Then through the selective chemical etching of (111) crystalline planes of silicon, each hole in the resist was transformed into an inverted pyramid with a basis angle of 54.7°, that between (100) and (111) planes in cubic system. Five different lattice periods were studied: 200, 350, 500, 600 and 750 nm. Their geometries are summarized in Table 1.

Fabrication of the mold: In order to make master surfaces hydrophobic, they were submitted to a UV-ozone treatment of 30 min, then placed inside a dryer with a silanizing agent (1H,1H,2H,2H perfluorodecyltrichlorosilane, ABCR) for 12 hours before being rinsed with isopropanol and distilled water, and dried. Then, the master pattern was replicated by moulding polydimethylsiloxane (PDMS, Sylgard 184 purchased from Neyco) on top. Once peeled, the PDMS replica was heated during 1 hour at 150°C to finish the crosslinking of the PDMS and make sure that there will be no interaction with the sol-gel layer during the nano-imprinting step.

Silica sol-gel layer: A methyltriethoxysilane (m-TEOS purchased from SigmaAldrich) solution at pH=2 was deposited by spin-coating (2000 rpm, 60s) on a Cerox cleaned glass sample (*Planiclear glass* from Saint-Gobain Glass, 2x2 cm^2) to achieve a homogenous 400 nm thick layer.

Nano-imprint: PDMS mold was then pressed (1 bar on 2x2 cm^2 sample) on a freshly spin-coated silica sol-gel layer during 1 hour while heating at 100°C to trigger silica condensation. After the mold removal, samples were annealed for 2 hours at 200°C followed by 1 hour at 500°C to remove remaining carbonaceous compounds and to densify the silica layer.

Magnetron sputtering: Thin conformal silver films (10-80 nm) were deposited at normal incidence from a pure target on flat or patterned silica surfaces with an industrial magnetron-sputtering machine (LINA350, Alcatel) with target size of about 30x15cm^2. The deposition was performed in direct current mode with argon at a speed 1.3nm/s and a power around 400W.

Dewetting condition: Immediately after deposition, samples were annealed in air at 400°C for 2h, inducing the solid-state dewetting.

Morphological study: An atomic force microscope (AFM, ICON from Bruker) was used in tapping-mode to characterize patterned surfaces (master and silica layer) and the thickness of silver layers. The morphology of dewetted film was characterized by scanning-electron microscopy (SEM, Gemini column, Zeiss) after Pt metallization. High resolution was favoured by an in-lens secondary electron detector. SEM experiments presented on Figure 6 were performed with a FEI Quanta 200 ESEM FEG apparatus in a 400 Pa oxygen atmosphere. A thermocouple placed close to the sample[51] allowed for an accurate control of the sample temperature. In this experiment sample was heated from 25°C to 350°C with a ramp of 50°C/s. The fast video rate (20 images/min) allowed following the dynamics of the dewetting front.

Optical characterization: Spectroscopic transmission and reflection measurements were performed at normal incidence with a Perkin Elmer λ950 apparatus equipped with an integrating sphere.

Optical numerical simulations: Maxwell equations were solved by the commercial finite-element-based software COMSOL Multiphysics [52]. The simulation domain consisted of a unit cell of the periodic structure, containing air as the superstrate and silica as the substrate

and a silver nanoparticle defined by a hemisphere in air and a cone in silica. The cone tip was rounded in order to reproduce the real experimentally-observed shape and also to decrease the errors related to the meshing defects. The structure was illuminated by a plane wave at normal incidence using an electromagnetic port. Periodic Floquet conditions were used on the borders orthogonal to the grating wave vector. A port in reflection or transmission was defined for each diffraction order. Convergence as a function of mesh size was carefully tested. Energy conservation was verified by checking if the sum of the power in all the modes (transmitted, reflected and dissipated by omhic losses) is equal to the incident power. The calculated absorption represents ohmic losses (Joule effect). Tabulated bulk dielectric functions of silica and silver were used.

Acknowledgements

Authors would like to thank Prof. Ingve Simonsen for inspiring discussions. This work was supported by the French National Research Agency (project FRAXOS, ANR-15-CHIN-0003). P.J. benefited from a CIFRE PhD grant funded by ANRT (Agence Nationale de la Recherche et de la Technologie) and by Saint-Gobain Recherche Paris.

Received: ((will be filled in by the editorial staff))
Revised: ((will be filled in by the editorial staff))
Published online: ((will be filled in by the editorial staff))

References

[1] H. A. Atwater, A. Polman, *Nat. Mater.* **2010**, *9,* 205.

[2] H. Tan, R. Santbergen, A. H. M. Smets, M. Zeman, *Nano Lett.* **2012**, *12*, 4070−4076.

[3] N. Kalfagiannis, A. Siozios, D. V. Bellas, D. Toliopoulos, L. Bowen, N. Pliatsikas, W. M. Cranton, C. Kosmidis, D. C. Koutsogeorgis, E. Lidorikis, et al., *Nanoscale* **2016**, *8,* 8236.

[4] J. N. Anker, W. P. Hall, O. Lyandres, N.C. Shah, J. Zhao, R. P. Van Duyne, *Nat. Mater.* **2008**, *7*, 442.

[5] A. J. Haes, L. Chang, W. L. Klein, R. P. Van Duyne, *J. Am. Chem. Soc.* **2005**, *127*, 2264.

[6] M. Altomare, N. T. Nguyen, and P. Schmuki, *Chem. Sci.* **2016**, *7*, 6865–6886.

[7] G. Baffou, R. Quidant, *Laser Photon Rev.* **2013**, *7*, 171–187.

[8] G. M. Akselrod, J. Huang, T. B. Hoang, P. T. Bowen, L. Su, D. R. Smith and M. H. Mikkelsen, *Adv. Mater.* **2015,** *27*, 8028-8034.

[9] D. Wang, Y. Ankun, A. J. Hryn, G. C. Schatz, T.W. Odom, *ACS Photonics* **2015** *2* 1789.

[10] A. D. Humphrey, W. L. Barnes, *J. Opt.* **2016,** *18*, 035005.

[11] N. C. Lindquist, P. Nagpal, K. M. McPeak, D. J. Norris and S.-H. Oh, *Rep. Prog. Phys.* **2012,** *75*, 036501.

[12] M. R. Gonçalves, *J. Phys. D: Appl. Phys.* **2014**, *47*, 213001.

[13] Y. He, J. Fu, Y. Zhao, *Front Phys.* **2014**, *9*, 47–59.

[14] R. A. Ganeev, U. Chakravarty, P. A. Naik, H. Srivastava, C. Mukherjee, M. K. Tiwari, R. V. Nandedkar, and P. D. Gupta, *Appl. Optics* **2007**, *46* ,1205-1210.

[15] T. R. Jensen, M.D. Malinsky, C. L. Haynes, R. P. Van Duyne, *J. Phys. Chem. B* **2000**, *104*, 10549-10556.

[16] S.-J. Jeong, J. Y. Kim, B. H. Kim, H.-S. Moon, S. O. Kim, *Mater. Today* **2013**, *16*, 468-476.

[17] D. Chateau, A. Liotta, F. Vadcard, J. Navarro, F. Chaput, J. Lermé, F. Lerouge, S. Parola, *Nanoscale* **2015**, *7*, 1934.

[18] L. M. Liz-Marzan, *Mater. Today* **2004**, *7*, 26–31.

[19] N. K. Kwon, T. K. Lee, S. K. Kwak, S. Y. Kim, *ACS Appl. Mater. Interfaces* **2017**, *9*, 39688–39698.

[20] W. Gotschy, K. Vonmetz, A. Leitner, F. R. Aussenegg, *Appl. Phys. B* **1996,** *63*, 381-384.

[21] A. I. Kuznetsov, J. Koch, B. N. Chichkov, *Opt. Express* **2009**, *17*, 18820–18825.

[22] A. I. Kuznetsov, C. Unger, J. Koch, B. N. Chichkov, *Appl. Phys. A* (**2012**), *106*, 479–487.

[23] N. Liu, H. Guo, L. Fu, S. Kaiser, H. Schweizer, H. Giessen, *Nature Mater.* **2008,** *7*, 31–7.

[24] C.V. Thompson, *Annu. Rev. Mater. Res.* **2012**, *42*, *399.*

[25] A. Kosinova, L. Klinger, O. Kovalenko and E. Rabkin, *Scripta Mater.* **2014**, *82*, 33-3.

[26] P. Jacquet, R. Podor, J. Ravaux, J. Lautru, J. Teisseire, I. Gozhyk, J. Jupille, R. Lazzari, *Acta Mater.* **2017,** *143*, 281.

[27] G. Atiya, D. Chatain, V. Mikhelashvili, G. Eisenstein, W.D. Kaplan, *Acta Mater.* **2014**, *81*, 304–314.

[28] G. Atiya, V. Mikhelashvili, G. Eisenstein, W.D. Kaplan, *J. Mater. Sci.* **2014**, *49*, 3863–3874.

[29] A. L. Giermann, C. V. Thompson, *Appl. Phys. Lett.* **2005**, *86*, 121903.

[30] A. L. Giermann, C. V. Thompson, *J. of Appl. Phys.* **2011**, *109*, 083520.

[31] P. Jacquet, R. Podor, J. Ravaux, J. Teisseire, I. Gozhyk, J. Jupille, R. Lazzari, *Scripta Mater.* **2016,** *115*, 128.

[32] E. Jiran and C. Thompson, *J. Electron. Mater.* **1990,** *19*, 1153.

[33] J. Kwon, T. Yoon, K. Kim and S. Min, *J. Appl. Phys.* **2003,** *93*, 3270.

[34] E. Presland, G. Price and D. Trimm, *Surf. Sci.* **1973,** *29*, 424.

[35] S. Sharma et J. Spitz, *Thin Solid Films* **1980**, *65*, 339.

[36] S. Morawiec, M. J. Mendes, S. Mirabella, F. Simone, F. Priolo, I. Crupi, *Nanotechnology.* **2013,** *24*, 265601.

[37] Y.-J. Oh, C. A. Ross, Y. S. Jung, Y. Wang, C. V. Thompson, *Small* **2009**, *5*, 860.

[38] S. K. Yang , F. Xu , S. Ostendorp , G. Wilde, H. P. Zhao, *Adv. Funct. Mater.* **2011**, *21*, 2446–2455.

[39] M. Yoshino, H. Osawa, A. Yamanaka, *Journal of Manufacturing Processes* **2012,** *14*, 478-486.

[40] J. Ye, C. V. Thompson, *Adv Mater.* **2011,** *23*, 1567-1571.

[41] J. Ye, *Sci. Rep.* **2015,** *5*, 9823.

[42] A. Le Bris, F. Maloum, J. Teisseire, F. Sorin, *Appl. Phys. Lett.* **2014**, *20*, 203102.

[43] W. D Kaplan, D. Chatain, P. Wynblatt, and W.C. Carter, *J. Mater. Sci*. **2013**, *48*, 5681.

[44] A. L. Dubov, K. Perez-Toralla, A. Letailleur, E. Barthel and J. Teisseire, J. *Micromech. Microeng.* **2013,** *23*, 125013.

[45] S. Stankic, R. Cortes-Huerto, N. Crivat, D. Demaille, J. Goniakowski, and J. Jupille, *Nanoscale* **2013**, *5*, 2448.

[46] C.T. Campbell, *Surf. Sci. Rep.* **1997**, *27*, 1.

[47] D. Chatain, F. Chabert, V. Ghetta, J. Fouletier, *J. Am. Ceram. Soc.* **1994**, *77*, 197.

[48] J.A. Thornton, J.A., J. Vac. Sci. Tech, **1974**, 11, 66

[49] C. L. Haynes, A. D. McFarland, L. Zhao, R. P. Van Duyne, G. C. Schatz, L. Gunnarsson, J. Prikulis, B. Kasemo, M. Kall, *J. Phys. Chem. B* **2003,** *107*, 7337-7342.

[50] B. Auguie, W. L. Barnes, *Phys. Rev. Lett.* **2008**, *101*, 143902.

[51] R. Podor, D. Pailhon, J. Ravaux, H.-P. Brau, *Microsc. Microanal.* **2015,** *21*, 307–312.

[52] M. W. Kennedy, S. Akhtar, J. A. Bakken, and R. E. Aune, H. A. Atwater, A. Polman, *COMSOL Users Conference, Stuttgart Germany*, **2011**.